Trajectory Tracking And Tether Tension Control Of Tethered Aerial Vehicle Using Nonlinear Model Predictive Control

Vicko Prkačin[a,*], Ivana Palunko[a], Ivan Petrović[b]

[a]*Laboratory for Intelligent Autonomous Systems (LARIAT), Faculty of Electrical Engineering and Applied Computing, University of Dubrovnik, Ćira Carića 4, Dubrovnik, 20000, Croatia*

[b]*Laboratory for Autonomous Systems and Mobile Robotics (LAMOR), Faculty of Electrical Engineering and Computing, University of Zagreb, Unska 3, Zagreb, 10000, Croatia*

Abstract

Tethered unmanned aerial vehicles are an effective solution for applications demanding extended flight durations. However, these systems exhibit complex nonlinear dynamics and coupling effects, which are further amplified in scenarios where the ground component of the system - Launch and Recovery System (LARS) is mounted on a mobile platform. In this study, the UAV has the task of following a user-defined trajectory while keeping the tether interaction force and the tether length within safe operating limits. This results in a nonlinear control problem that is subject to constraints. To solve this problem, a Nonlinear Model Predictive Control (NMPC) for the tethered aerial system is proposed in this paper. State estimation is achieved by capturing the tether interaction force using a minimal proprioceptive sensing system. It is further demonstrated that active tether force control can improve estimation accuracy. Finally, the proposed control and estimation strategies are implemented and validated experimentally on a UAV-LARS system.

Keywords: Tethered aerial vehicle, Nonlinear Model Predictive Control, Coordinated control, Minimal proprioceptive sensing

1. Introduction

Unmanned aerial vehicles (UAVs) have seamlessly integrated into modern society thanks to innovation and reduced costs, and are now an essential tool across a wide range of industries. Despite continuous advances in battery technology aimed at improving energy density, flight time remains the key limiting factor for the wider adoption of these systems. Tethered aerial systems have emerged as an ad hoc solution to overcome this limitation. Unlike conventional UAVs, they are physically connected to a ground station that provides them with a continuous power supply and a robust data transmission link. This makes tethered systems ideal candidates for applications that require extended uptime, such as telecommunications [1], monitoring in harsh environments [2], or even art creation [3].

However, due to the complex nonlinear dynamics and interactions within the coupled multibody system, tethered aerial systems introduce a unique set of challenges. As they gain prominence in industrial applications, the development of autonomous solutions and advanced coordinated control is identified as essential for enhancing their effectiveness and operational safety [4]. Consequently, this area has gained significant interest and remains an active field of research.

In tethered aerial systems, the main control challenge is to achieve accurate tracking of the UAV's reference position while managing tether interaction forces and ensuring operational safety. The work in [5] demonstrated how the control of tether interaction forces can enhance the UAV stability while in hover when subjected to external disturbances. This improvement was achieved using a combination of proportional-integral-derivative (PID) control and dynamic inversion techniques. Similarly, in [6], geometric control is employed to track the desired position and ensure asymptotic stabilization of UAVs tethered to a fixed point. A more complex scenario involving a UAV tethered to a moving platform is presented in [7], where a control strategy based on dynamic feedback linearization is proposed to track both UAV position references and tether interaction forces. Further expanding on this work, the authors in [8] provide a detailed overview of the modelling and state estimation techniques for the tethered aerial system.

In contrast to the aforementioned publications, which emphasized maintaining a taut tether, several other studies have explored slack tether management strategies. This approach aims to decouple the motion between the tethered system components and minimize power consumption by mitigating the interaction force exerted by the tether. A non-taut tether management strategy for UAV-USV coordination, based on static catenary cable theory, was proposed in [9]. To mitigate issues like excessive slack or tension in the tether, the authors further developed a smart reel system for dynamic tether length regulation, as detailed in [10]. Another non-taut cable strategy focusing on cable-guided landing on a moving platform utilizing continuous velocity vector fields is discussed in [11].

In the domain of relative localization for heterogeneous robot teams, the focus is traditionally on vision-based feedback [12],[13]. In tethered UAV systems, state estimation methods

*Corresponding author.
E-mail address: vicko.prkacin@unidu.hr (Vicko Prkačin)

can further exploit knowledge of tether behaviour to improve estimation accuracy. Based on the underlying model assumptions, they are generally classified into taut and non-taut tether approaches. Similar to control methods, non-taut tether approaches often use tether shape modelling. For instance, studies in [14, 15, 16] applied catenary cable models along with tether length and direction sensing to estimate the UAV's position relative to a fixed point. In contrast, taut tether strategies usually involve a more extensive sensor suite for state estimation. In [17], a combination of magnetic encoders and load sensors was used to estimate the tether state for precise helicopter landings on moving platforms. Similarly, [18] utilized encoder measurements to develop a tethered UAV system suited for inspection in GPS-denied environments. In an attempt to minimize reliance on dedicated sensors, some researchers have focused on estimating relative position by sensing tether interaction forces. For example, [19] proposed an Unscented Kalman Filter (UKF) using aircraft inertial measurement unit (IMU) measurements for position estimation relative to a static platform. A method is further examined in [20]. Despite these advancements, there is still a lack of experimental studies specifically addressing state estimation for UAVs tethered to moving platforms, leveraging minimal sensor configurations.

This paper presents a coordinated control system for an autonomous tethered aerial vehicle system. This system is part of a larger heterogeneous autonomous robotic framework for underwater marine litter search, identification, and collection, developed as part of the SeaClear[1] and SeaClear2.0[2] projects. A major challenge for the autonomous system operating in the underwater environment is localization, which is hampered by the absence of a Global Positioning System (GPS) and the inherent limitations of underwater vision-based methods. Previous research [21], [22] has demonstrated that intermittent vision updates from a UAV can improve the localization of underwater vehicles by providing accurate position information. However, this process requires prolonged flight durations, making conventional battery-powered UAVs unsuitable for the task, and driving the development of an autonomous tethered aerial vehicle system.

An autonomous tethered aerial vehicle system includes two segments: an unmanned aerial vehicle (UAV) and its Launch and Recovery System (LARS). The UAV, a unidirectional-thrust multirotor platform, is tethered to the LARS, which provides power, communication, and tether management system (TMS). Designed as a compact, standalone unit, the LARS can be deployed from various platforms, including ground vehicles, ships, or autonomous unmanned surface vehicles (USVs).

In the proposed use case, the UAV is tasked with tracking the user-defined position reference relative to LARS mounted on a moving platform. At the same time, TMS regulates the tether interaction force to prevent excessive pull or, in contrast, excessive slack that can lead to entanglements. Consequently, the development of coordinated control is necessary to meet the end-user requirements and ensure operational safety. Given the inherent ability to handle multiple inputs-multiple outputs and performance benefits, Model Predictive Control (MPC) has emerged as a widely adopted control strategy for heterogeneous robotic teams. In the free-flight aerial applications, MPC has been successfully applied to various track-and-land scenarios, either for path planning [23] or direct control [24]. In the tethered aerial applications, MPC has been employed as a high-level controller for the coordination of a system of tethered UAVs [25] and in a heterogeneous robotic UAV-USV team for collaborative object manipulation [26].

To address the increased complexity arising from the coupled dynamics and strong nonlinearities of the tethered aerial system in the outlined use case, the control strategy based on the Nonlinear Model Predictive Control (NMPC) is proposed. Compared to classic methods, NMPC offers several key advantages, including the ability to impose constraints on system states and inputs. By carefully constraining the state variables, NMPC can enforce local geo-fencing to prevent the UAV from entering regions of potential entanglement, such as near masts, antennas, or parts of the USV superstructure. At the same time, it can guarantee the maximum tether length is not exceeded and that the interaction force between the UAV and LARS is maintained within safe operational limits. In the prior research [27],[28], it was demonstrated that the tether interaction force can be observed in the UAV's existing onboard sensors. Building on this concept, the state estimation based on UAV proprietary sensing and LARS encoder measurements is proposed. It will be further shown how estimation accuracy can be enhanced through active control of the tether interaction force. Finally, the proposed algorithms are implemented and experimentally verified on the custom LARS developed within the SeaClear project.

The contributions of this paper are outlined as follows:

1. Nonlinear Model Predictive control for trajectory tracking of the tethered aerial vehicle position relative to the non-stationary launch and recovery system,

2. Extended Kalman Filter for the estimation of the position of the tethered aerial vehicle relative to the non-stationary launch and recovery system, based on the aerial vehicle's proprietary sensors and launch and recovery system's motor encoder measurements,

3. Tether tension control framework for the enhancement of the estimation accuracy,

4. Implementation and experimental validation of the proposed algorithms on a real-world UAV launch and recovery system.

The remainder of the paper is structured into the subsequent sections. Section 2 outlines the kinematics and dynamics of the system. Section 3 describes the Nonlinear Model Predictive Controller. Section 4 presents the proposed estimator. Implementation of the experimental setup is discussed in Section 5, with experimental results presented in Section 6. Finally, Section 7 provides concluding remarks and suggests future research directions.

[1] SeaClear Project - https://seaclear-project.eu/

[2] SeaClear2.0 Project - https://www.seaclear2.eu/

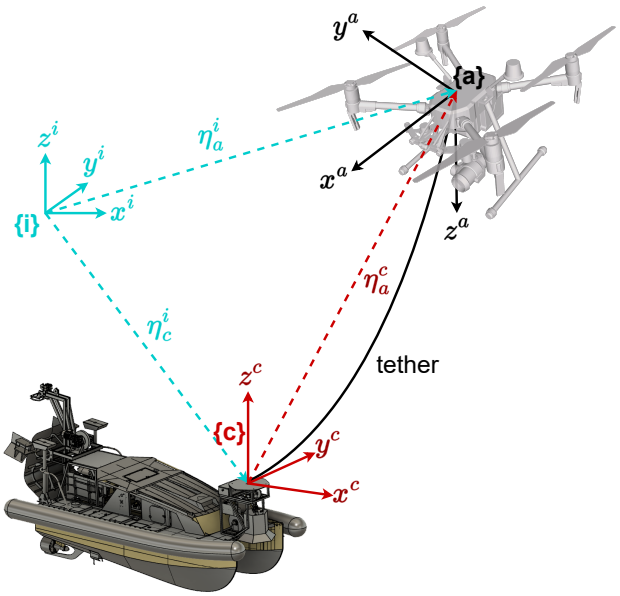


Figure 1: Coordinate system representation for the unmanned aerial vehicle (UAV) tethered to a launch and recovery system (LARS), mounted on an unmanned surface vehicle (USV): Inertial coordinate frame is denoted $\{i\}$. The aircraft coordinate frame is denoted $\{a\}$ and fixed to the aircraft's centre of gravity. The LARS coordinate frame is denoted $\{c\}$.

2. Modelling of tethered unmanned aerial vehicle

2.1. Kinematics

In this work, a system consisting of a tethered unmanned aerial vehicle (UAV) and a respective launch and recovery system (LARS) mounted on a moving platform is examined. The variable tether length scenario is considered. Specifically, on the LARS, a tether management system is present, equipped with a cylinder-shaped actuator whose rotational motion leads to the variation in the tether length.

An inertial coordinate frame $\{i\}$, aircraft fixed coordinate frame $\{a\}$ assumed to be attached to the centre of gravity, and a LARS fixed coordinate system $\{c\}$ are defined. The system, mounted on an unmanned surface vehicle (USV), is illustrated in Fig. 1. Orientation of the aircraft frame relative to the inertial frame is described by rotation matrix $\mathbf{R}_a^i$, obtained according to Z-Y-X convention:

$$\mathbf{R}_a^i = \mathbf{R}_{z,\psi}\mathbf{R}_{y,\theta}\mathbf{R}_{x,\phi},$$

where ϕ, θ and ψ represent Euler angles *roll*, *pitch* and *yaw* respectively, and $\mathbf{R}_{z,\psi}\mathbf{R}_{y,\theta}\mathbf{R}_{x,\phi}$ are three principal rotations matrices

$$\mathbf{R}_{x,\phi} = \begin{bmatrix} 1 & 0 & 0 \\ 0 & \cos(\phi) & -\sin(\phi) \\ 0 & \sin(\phi) & \cos(\phi) \end{bmatrix},$$

$$\mathbf{R}_{y,\theta} = \begin{bmatrix} \cos(\theta) & 0 & \sin(\theta) \\ 0 & 1 & 0 \\ -\sin(\theta) & 0 & \cos(\theta) \end{bmatrix},$$

$$\mathbf{R}_{z,\psi} = \begin{bmatrix} \cos(\psi) & -\sin(\psi) & 0 \\ \sin(\psi) & \cos(\psi) & 0 \\ 0 & 0 & 1 \end{bmatrix}.$$

Note the mismatch of the z axis orientation in the $\{i\}$ and $\{a\}$ frame, outlined in Fig. 1. Therefore, additional fixed transformation $\mathbf{R}_T$ is performed

$$\mathbf{R}_a^i = \mathbf{R}_T\mathbf{R}_a^i,$$

where

$$\mathbf{R}_T = \begin{bmatrix} 1 & 0 & 0 \\ 0 & -1 & 0 \\ 0 & 0 & -1 \end{bmatrix}.$$

As defined, $\mathbf{R}_a^i$ transforms vector in the $\{a\}$ frame, to $\{i\}$ frame, that is

$$v^i = \mathbf{R}_a^i v^a.$$

Association of Euler rates to aircraft angular velocity is defined as

$$\dot{\xi}_a = \mathbf{T}\omega_a^a, \tag{1}$$

where

$$\mathbf{T} = \begin{bmatrix} 1 & \sin(\phi)\tan(\theta) & \cos(\phi)\tan(\theta) \\ 0 & \cos(\phi) & -\sin(\phi) \\ 0 & \frac{\sin(\phi)}{\cos(\theta)} & \frac{\cos(\phi)}{\cos(\theta)} \end{bmatrix}.$$

In a similar fashion, this time without additional $\mathbf{R}_T$ transformation, the LARS orientation is given by $\mathbf{R}_c^i$.

Components of the tethered UAV system are related by the following vectors and parameters:
$\eta_a^i \in \mathbb{R}^{3\times1}$ - position of the origin of $\{a\}$ expressed in $\{i\}$,
$\eta_c^i \in \mathbb{R}^{3\times1}$ - position of the origin of $\{c\}$ expressed in $\{i\}$,
$\eta_a^c \in \mathbb{R}^{3\times1}$ - position of the origin of $\{a\}$ expressed in $\{c\}$,
$d^c \in \mathbb{S}^2$ - unit vector in the tether direction expressed in $\{c\}$,
$\xi_a \in \mathbb{R}^{3\times1}$ - vector of aircraft Euler angles,
$\xi_c \in \mathbb{R}^{3\times1}$ - vector of LARS Euler angles,
$v_a^a \in \mathbb{R}^{3\times1}$ - linear velocity of $\{a\}$ with respect to $\{i\}$ expressed in $\{a\}$,
$v_c^c \in \mathbb{R}^{3\times1}$ - linear velocity of $\{c\}$ with respect to $\{i\}$ expressed in $\{c\}$,
$\omega_a^a \in \mathbb{R}^{3\times1}$ - angular velocity of $\{a\}$ with respect to $\{i\}$ expressed in $\{a\}$,
$\omega_c^c \in \mathbb{R}^{3\times1}$ - angular velocity of $\{c\}$ with respect to $\{i\}$ expressed in $\{c\}$,
$\mathbf{\Omega}_c \in \mathbb{R}^{3\times3}$ - skew-symmetric matrix associated to ω_c^c,
$\theta_w \in \mathbb{R}$ - winch actuator angular position,
$\tau_a \in \mathbb{R}^{3\times1}$ - aircraft moment about its center of gravity expressed in $\{a\}$,
$\mathbf{I}_a \in \mathbb{R}^{3\times3}$ - aircraft inertia matrix about its center of gravity,
$J_w \in \mathbb{R}^+$ - winch actuator inertia,
$r_w \in \mathbb{R}^+$ - winch actuator radius,
$m_a \in \mathbb{R}^+$ - aircraft mass,
$l \in \mathbb{R}_0^+$ - tether length,
$g \in \mathbb{R}^+$ - acceleration of gravity,
$F_t \in \mathbb{R}^+$ - magnitude of the aircraft thrust force,
$F_l \in \mathbb{R}_0^+$ - magnitude of the tether tension force,
$\tau_w \in \mathbb{R}$ - winch actuator input torque.

To simplify the system model, the following assumptions are introduced, deviating from the most general case:

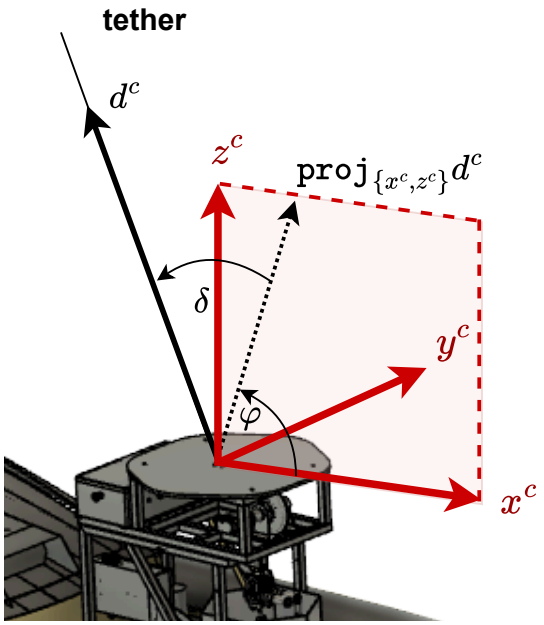


Figure 2: LARS coordinate system and tether angles definition. Elevation angle φ is the angle between the projection of d^c on $\{x^c, z^c\}$ plane and x^c. Azimuth angle δ is the angle between d^c and the plane $\{x^c, z^c\}$

Assumption 1. - *Tether attachment point is in the aircraft frame origin. Therefore, aircraft rotational dynamics are unaffected by the tether tension force.*

Assumption 2. - *Aircraft design is symmetric. Therefore, aircraft inertia matrix* $\mathbf{I}^a$ *is diagonal.*

Assumption 3. - *LARS is considered to be an independent subsystem unaffected by the aircraft dynamics, with states available as measurements at all times. It supports both translational and rotational motion, as when mounted on an unmanned surface vehicle (USV).*

Now, following the work in [8], the unit vector d^c in the tether direction is defined. Under the taut tether assumption, this will allow aircraft position to be expressed relative to the LARS as η_a^c. The unit vector d^c is parameterized by the elevation angle, $\varphi \in [0, 2\pi]$, and the azimuth angle, $\delta \in \left[-\frac{\pi}{2}, \frac{\pi}{2}\right]$, as

$$d^c = \begin{bmatrix} \cos(\delta)\cos(\varphi) \\ -\sin(\delta) \\ \cos(\delta)\sin(\varphi) \end{bmatrix}. \tag{2}$$

The azimuth angle δ is defined as the angle between d^c and the plane $\{x^c, z^c\}$, and the elevation angle φ as the angle between projection of d^c on $\{x^c, z^c\}$ and x^c, as depict in Fig. 2.

Therefore, the position of the aircraft in $\{c\}$ is

$$\eta_a^c = d^c l,$$

and in $\{i\}$, accordingly

$$\eta_a^i = \eta_c^i + \mathbf{R}_c^i d^c l. \tag{3}$$

The aircraft's linear velocity in the inertial frame is obtained by the differentiation of the previous equation

$$\dot{\eta}_a^i = \mathbf{R}_c^i \left(v_c^c + l\boldsymbol{\Omega}_c d^c + \dot{l}d^c + l\dot{d}^c\right). \tag{4}$$

Note that relation $\dot{\eta}_c^i = \mathbf{R}_c^i v_c^c$ is exploited. The aircraft inertial acceleration is obtained by additional differentiation of (4), leading to

$$\begin{aligned} \ddot{\eta}_a^i = \mathbf{R}_c^i \big[&\boldsymbol{\Omega}_c \left(v_c^c + l\boldsymbol{\Omega}_c d^c + 2\dot{l}d^c + 2l\dot{d}^c\right) \\ &+ \dot{v}_c^c + l\dot{\boldsymbol{\Omega}}_c d^c + 2\dot{l}\dot{d}^c + \ddot{l}d^c + l\ddot{d}^c\big]. \end{aligned} \tag{5}$$

Finally, the variables $q \in \mathbb{R}^{3\times 1}$ and $\mathbf{J}_q \in \mathbb{R}^{3\times 3}$ are defined as

$$q = \begin{bmatrix} l \\ \varphi \\ \delta \end{bmatrix}, \tag{6}$$

$$\mathbf{J}_q = \begin{bmatrix} \cos(\delta)\cos(\varphi) & -l\cos(\delta)\sin(\varphi) & -l\cos(\varphi)\sin(\delta) \\ -\sin(\delta) & 0 & -l\cos(\delta) \\ \cos(\delta)\sin(\varphi) & l\cos(\delta)\cos(\varphi) & -l\sin(\delta)\sin(\varphi) \end{bmatrix},$$

and substituted into (5), resulting in

$$\begin{aligned} \ddot{\eta}_a^i = \mathbf{R}_c^i \big[&\boldsymbol{\Omega}_c \left(v_c^c + l\boldsymbol{\Omega}_c d^c + 2\mathbf{J}_q\dot{q}\right) \\ &+ \dot{v}_c^c + l\dot{\boldsymbol{\Omega}}_c d^c + \dot{\mathbf{J}}_q\dot{q} + \mathbf{J}_q\ddot{q}\big]. \end{aligned}$$

To shorten this lengthy expression, a new variable a_c is introduced

$$a_c = \boldsymbol{\Omega}_c \left(v_c^c + l\boldsymbol{\Omega}_c d^c + 2\mathbf{J}_q\dot{q}\right) + \dot{v}_c^c + l\dot{\boldsymbol{\Omega}}_c d^c + \dot{\mathbf{J}}_q\dot{q},$$

leading to

$$\ddot{\eta}_a^i = \mathbf{R}_c^i \left(a_c + J_q\ddot{q}\right). \tag{7}$$

2.2. Newton-Euler equations

The aircraft considered in this paper is a unidirectional-thrust vehicle, meaning that thrust force is produced only in the $-z_a$ direction of the aircraft fixed coordinate frame. A general aircraft motion through space is then achieved by directing the thrust via a change of vehicle orientation.

For the given system, the translational dynamics of the aircraft in the inertial frame are as follows

$$m_a\ddot{\eta}_a^i = -\mathbf{R}_a^i \begin{bmatrix} 0 \\ 0 \\ F_t \end{bmatrix} - \begin{bmatrix} 0 \\ 0 \\ m_a g \end{bmatrix} - F_l \mathbf{R}_c^i d^c. \tag{8}$$

Under the declared assumptions, aircraft rotational dynamics are

$$\mathbf{I}_a\dot{\omega}_a^a = \mathbf{I}_a\omega_a^a \times \omega_a^a + \tau_a. \tag{9}$$

As stated in the introduction, the case where the tether management system is available is considered. This system is composed of a rotational actuator (motor) coupled with a cylinder. When the motor applies an input torque, the tether is wound or unwound on the cylinder, depending on the direction of the applied torque. Under the mild assumption that changes in actuator inertia and radius are negligible, the tether actuator dynamic is

$$J_w\ddot{\theta}_w = \tau_w + F_l r_w.$$

Moreover, using the identity $l = r_w\theta_w$, the dynamics of the tether length are obtained

$$\frac{J_w}{r_w}\ddot{l} = \tau_w + F_l r_w. \tag{10}$$

In the scope of this paper, the aim is to estimate and control the relative position of the aircraft with respect to the LARS. This relative position is captured in (6), and characterized by the tether length, azimuth, and elevation angles. Thus, the dynamics of this variable are derived next.
To start, (7) is substituted into (8), which, after some rearrangements, results in

$$m_a\mathbf{J}_q\ddot{q} + F_l d^c = -f_c - f_t - f_g, \tag{11}$$

where elements

$$f_c = m_a a_c, \quad f_t = \mathbf{R}_i^c\mathbf{R}_a^i\begin{bmatrix}0\\0\\F_t\end{bmatrix}, \quad f_g = \mathbf{R}_i^c\begin{bmatrix}0\\0\\m_a g\end{bmatrix},$$

are introduced to shorten the notation. By combining (11) and (10), a subsequent system is formed

$$\begin{bmatrix} m_a\mathbf{J}_q & d^c \\ \begin{bmatrix}\frac{J_w}{r_w} & 0 & 0\end{bmatrix} & -r_w \end{bmatrix}\begin{bmatrix}\ddot{q}\\ F_l\end{bmatrix} = \begin{bmatrix}-f_c - f_t - f_g\\ \tau_w\end{bmatrix}.$$

Here, for brevity, a matrix $\mathbf{M} \in \mathbb{R}^{4\times4}$ is defined as

$$\mathbf{M} = \begin{bmatrix} m_a\mathbf{J}_q & d^c \\ \begin{bmatrix}\frac{J_w}{r_w} & 0 & 0\end{bmatrix} & -r_w \end{bmatrix}.$$

It is important to mention the singularity of the matrix at $l = 0$ or $|\delta| = \frac{\pi}{2}$. However, this is merely a theoretical concern, as in practice, it is unlikely for the system to reach that state. Considering this, the complete system dynamics are finally given as

$$\begin{aligned}\ddot{q} &= \begin{bmatrix}\mathbf{I}^{3\times3} & 0^{3\times1}\end{bmatrix}\mathbf{M}^{-1}\begin{bmatrix}-f_c - f_t - f_g\\ \tau_w\end{bmatrix},\\ F_l &= \begin{bmatrix}0^{1\times3} & 1\end{bmatrix}\mathbf{M}^{-1}\begin{bmatrix}-f_c - f_t - f_g\\ \tau_w\end{bmatrix},\end{aligned} \tag{12}$$

where $\mathbf{I}^{3\times3}$, $0^{3\times1}$ and $0^{1\times3}$ are the identity matrix and zero vectors.

3. Nonlinear Model Predictive Controller

In this section, a Nonlinear Model Predictive Controller for UAV trajectory tracking and tether interaction force control is described. First, the system model for controller design is delineated in Subsection 3.1. Later on, the NMPC controller is formulated in Subsection 3.2.

3.1. Plant model

The plant state vector $x \in \mathbb{R}^{12\times1}$, control input vector $u \in \mathbb{R}^{5\times1}$, vector of LARS states $d \in \mathbb{R}^{15\times1}$ regarded as the vector of measured disturbances, and output vector $y \in \mathbb{R}^{12\times1}$ are respectively defined as

$$\begin{aligned}x &= \begin{bmatrix}q & \dot{q} & \xi_a & \omega_a^a\end{bmatrix}^T,\\ u &= \begin{bmatrix}\tau_w & F_t & \tau_a\end{bmatrix}^T,\\ d &= \begin{bmatrix}v_c^c & \dot{v}_c^c & \xi_c & \omega_c^c & \dot{\omega}_c^c\end{bmatrix}^T,\\ y &= \mathbf{I}x,\end{aligned}$$

where $\mathbf{I} \in \mathbb{R}^{12\times12}$ is the identity matrix. Hence, the nonlinear plant model is

$$\begin{aligned}\dot{x} &= f(x,u,d),\\ \dot{x} &= \begin{bmatrix}\dot{q} & \ddot{q} & \dot{\xi}_a & \dot{\omega}_a^a\end{bmatrix}^T,\end{aligned} \tag{13}$$

where $\ddot{q}, \dot{\xi}_a$ and $\dot{\omega}_a^a$ are stated in (12), (1), (9), respectively.

3.2. Controller formulation

Nonlinear Model Predictive Controller, at each control interval k, calculates control action over the prediction horizon $p \in \mathbb{R}_0^+$, that minimize cost function J_k while satisfying input and state constraints. Only the first control input is then applied to the system, and the process is repeated in a receding horizon manner. This optimization problem is a nonlinear program, defined as

$$\begin{aligned}J_k^*(x_k,u_k) \coloneqq \min_{\mathrm{U}} \sum_{i=0}^{p-1}\Big[&\left(e_{y_{k+i}}^T\mathbf{Q}e_{y_{k+i}}\right) + \left(e_{u_{k+i}}^T\mathbf{R}_u e_{u_{k+i}}\right)\\ &+ \left(\Delta u_{k+i}^T\mathbf{R}_{\Delta u}\Delta u_{k+i}\right)\Big] + \rho_\varepsilon\varepsilon_k^2\\ \text{subject to}\quad & x_{k+i+1} = f_d(x_{k+i},u_{k+i},d_k)\\ & x_{k+i} \in \mathcal{X}\\ & u_{k+i} \in \mathcal{U}\\ & x_0 = x(0)\end{aligned} \tag{14}$$

where

$$\begin{aligned}\mathrm{U} &= \begin{bmatrix}u_k & u_{k+1} & \dots & u_{k+p-1} & \varepsilon_k\end{bmatrix},\\ e_{y_{k+i}} &= \left(y_{r_{k+i+1}} - y_{k+i+1}\right),\\ e_{u_{k+i}} &= \left(u_{r_{k+i}} - u_{k+i}\right),\\ \Delta u_{k+i} &= \left(u_{k+i} - u_{k+i-1}\right).\end{aligned}$$

The remaining variables are listed below
$J_k^* \in \mathbb{R}_0^+$ - cost function value at time interval k,
$\mathrm{U} \in \mathbb{R}^{5\times p}$ - optimized control action over the prediction horizon,
$i \in \mathbb{R}^+$ - prediction horizon step,
$\varepsilon_k \in \mathbb{R}_0^+$ - constraint violation slack variable at time interval k,
$\rho_\varepsilon \in \mathbb{R}_0^+$ - constraint violation penalty weight,
$\mathbf{Q} \in \mathbb{R}^{12\times12} \mid \mathbf{Q} \succeq 0$ - output penalty weight matrix,
$\mathbf{R}_u \in \mathbb{R}^{5\times5} \mid \mathbf{R}_u \succeq 0$ - input penalty weight matrix,
$\mathbf{R}_{\Delta u} \in \mathbb{R}^{5\times5} \mid \mathbf{R}_{\Delta u} \succeq 0$ - input rate penalty weight matrix,

$\mathcal{X} \in \mathbb{R}^{12\times1}$ - set of the state constraints,
$\mathcal{U} \in \mathbb{R}^{5\times1}$ - set of the input constraints,
$f_d\left(x_{k+i}, u_{k+i}, d_k\right) \in \mathbb{R}^{12\times1}$ - discretized plant model,
$y_{k+i} \in \mathbb{R}^{12\times1}$ - predicted plant output at the i-th prediction horizon step,
$y_{r_{k+i}} \in \mathbb{R}^{12\times1}$ - output reference value at the i-th prediction horizon step,
$u_{r_{k+i}} \in \mathbb{R}^{5\times1}$ - input reference value at the i-th prediction horizon step,
$e_{y_{k+i}} \in \mathbb{R}^{12\times1}$ - predicted output tracking error at the i-th prediction horizon step,
$e_{u_{k+i}} \in \mathbb{R}^{5\times1}$ - predicted input tracking error at the i-th prediction horizon step,
$\Delta u_{k+i} \in \mathbb{R}^{5\times1}$ - input change between i-th and $(i-1)$-th prediction horizon step.

If both input and output constraints are set as hard constraints, meaning they must be met in the optimization problem, solving the optimization problem could become infeasible. In that case, some of the constraints can be designated as soft, meaning that the controller can deem a solution U optimal, despite the constraint violation. The constraint softening is achieved by introducing a slack variable ε_k for constraint violation as

$$x_{min} - \varepsilon_k x_{min} \leq x_{k+i} \leq x_{max} + \varepsilon_k x_{max},$$

where x_{min} and x_{max} are the state lower and upper bound. When the optimization problem is feasible, equivalence is achieved through the appropriate selection of the constraint violation penalty weight. As highlighted earlier, the LARS is treated as an independent system with available measurements but without a known model. Therefore, it is not possible to preview the measured disturbances, and they are assumed to remain constant throughout the prediction horizon, as indicated in (14).

3.3. Controller implementation

The aforementioned controller is implemented in MATLAB®SIMULINK with the Model Predictive Control Toolbox [29]. To start off, the continuous-time prediction model is defined as (13). Subsequently, the discretization of this model, achieved through the implicit trapezoidal rule, yields the discrete plant model f_d. A performance comparison with the Euler and fourth-order Runge-Kutta methods showed similar accuracy, with the latter having slower execution times, making the trapezoidal method the preferred option. At this point, the output vector is presumed to be available, and the matter of state estimation is addressed in the following section.

With five available inputs, it is possible to control either five outputs or inputs to track the desired trajectories. The selection is encoded in the weight matrices

$$\begin{aligned}\mathbf{Q} &= \mathrm{diag}(w_{y_1}^2, \ldots, w_{y_{12}}^2),\\ \mathbf{R}_u &= \mathrm{diag}(w_{u_1}^2, \ldots, w_{u_5}^2),\\ \mathbf{R}_{\Delta u} &= \mathrm{diag}(w_{\Delta u_1}^2, \ldots, w_{\Delta u_5}^2),\end{aligned}$$

with input and output weights, specified in Table 1. From the output weights, it is evident that control is applied to the UAV yaw angle ψ, and its relative position with respect to the LARS, i.e., q. This choice leaves one input unused, τ_w, which is utilized to control the tether tension force F_l. Specifically, given a reference tension force F_{l_r}, equation (10) is solved for τ_w. Since the $\ddot{l}$ is not readily available, $\dot{l}$ is filtered by a low-pass filter and differentiated to calculate the control input reference. Beyond the evident safety considerations, the control of the tension force enables additional operational flexibility. For instance, in scenarios where power consumption is a priority, non-taut tether management strategies, such as those based on catenary tether modelling, can be implemented. In contrast, for the taut-tether strategies, tether tension control can provide additional robustness to outside disturbances, or as further elaborated in Section 4, it can be employed for improved state estimation. Finally, aggressive control actions are penalized by setting the input rate weight $w_{\Delta u} = 0.1$, for all inputs.

Table 1: NMPC Weights and Constraints

Output parameters				
x	w_y	x_{min}	x_{max}	Unit
l	5	0.1	50	m
φ	5	0	2π	rad
δ	5	$-\frac{\pi}{2}$	$\frac{\pi}{2}$	rad
$\dot{l}$	0	-1.5	1.5	$\mathrm{m\,s^{-1}}$
$\dot{\varphi}$	0	$-\infty$	∞	$\mathrm{rad\,s^{-1}}$
$\dot{\delta}$	0	$-\infty$	∞	$\mathrm{rad\,s^{-1}}$
ϕ	0	$-\frac{\pi}{6}$	$\frac{\pi}{6}$	rad
θ	0	$-\frac{\pi}{6}$	$\frac{\pi}{6}$	rad
ψ	1	$-\pi$	π	rad
$\omega_{a_x}^a$	0	$-\frac{5\pi}{3}$	$\frac{5\pi}{3}$	$\mathrm{rad\,s^{-1}}$
$\omega_{a_y}^a$	0	$-\frac{5\pi}{3}$	$\frac{5\pi}{3}$	$\mathrm{rad\,s^{-1}}$
$\omega_{a_z}^a$	0	$-\frac{3\pi}{5}$	$\frac{3\pi}{5}$	$\mathrm{rad\,s^{-1}}$
Input parameters				
u	w_u	u_{min}	u_{max}	Unit
τ_w	10	-1.5	-0.15	N m
F_t	0	0	90	N
τ_{a_x}	0	-10	10	N m
τ_{a_y}	0	-10	10	N m
τ_{a_z}	0	-10	10	N m

Physical limitations of the system are represented by a set of state and input constraints

$$\begin{aligned}\mathcal{X} &= \left\{x \in \mathbb{R}^{12\times1} | x_{min} < x < x_{max}\right\},\\ \mathcal{U} &= \left\{u \in \mathbb{R}^{5\times1} | u_{min} < u < u_{max}\right\},\end{aligned}$$

each with minimum x_{min}, and maximum x_{max} value, as outlined in the Table 1. Constraints are predicated on the DJI Matrice 210v2 RTK [30], UAV model employed in both simulations and experimental validation. Input constraints for τ_w are determined from (10), at steady state $\ddot{l} = 0$, for the desired maximum and minimum tension force values.

With the input and output references, measurements, weight matrices, and constraints, in place, the Sequential Quadratic Programming (SQP) algorithm is employed to solve the optimization problem (14).

3.4. Numerical Simulation

The numerical simulations are performed in MATLAB®SIMULINK, with plant and controller parameters outlined in Table 2. With no available prediction model for the measured disturbances, it is not efficient to compute control actions over the entire prediction horizon. Preferably, control actions are optimized for a segment of the prediction horizon, and for the remainder control remains constant. The parameter that specifies the number of time steps within the prediction horizon, over which control actions are calculated is the control horizon, denoted p_c in Table 2. A time step corresponds to the controller sample time T_s.

Table 2: Plant and Controller parameters

Parameter	Value	Unit
m_a	5.234	kg
I_a	$\begin{bmatrix} 0.105 & 0 & 0 \\ 0 & 0.105 & 0 \\ 0 & 0 & 0.140 \end{bmatrix}$	$\mathrm{kg\,m^2}$
J_w	0.011	$\mathrm{kg\,m^2}$
r_w	0.150	m
T_s	0.1	s
p	18	
p_c	2	

In the simulation scenario, the LARS is mounted on USV which navigates under the influence of waves. The presence of waves is emulated by oscillating roll, pitch, yaw, and heave motion. Its states, as delineated in Fig. 3, are generated in SIMULINK and assumed to be measured disturbances for the NMPC. Simultaneously, the UAV is tasked with tracking the reference trajectory relative to the LARS, while the tether tension force is controlled through τ_w. Tracking results for both the inputs and outputs obtained in the numerical simulation are illustrated in Fig. 4. The UAV and LARS ENU positions, alongside the reference trajectory transformed into the ENU frame, are outlined in Fig. 5. Presented results indicate the capability of the controller to cope with the unpredictable USV motion and waves, while satisfying the input and output constraints, therefore validating the viability of the proposed control approach.

4. State Estimation

In the preceding section, the availability of an output vector required by the NMPC was assumed. In this section, the absence of this vector is addressed by introducing an Extended Kalman Filter (EKF) for state estimation. The EKF is formulated to estimate relative aircraft position and velocity, namely q and $\dot{q}$, along with the tension force F_l. Estimation of aircraft orientation and angular velocity is extensively covered in the literature, therefore it is omitted in this segment for brevity.

4.1. Estimator formulation

An estimator state $x_e \in \mathbb{R}^{7\times 1}$ is defined as

$$x_e = \begin{bmatrix} F_l & q & \dot{q} \end{bmatrix}^T.$$

The state transition of q and $\dot{q}$ is represented by a discrete white noise acceleration model, while the state transition of the tension force is modelled as a random walk process. The estimator process model is accordingly

$$x_{e_{k+1}} = \mathbf{A}x_{e_k} + \Gamma v_k,$$

where $\mathbf{A} \in \mathbb{R}^{7\times 7}$ and $\Gamma \in \mathbb{R}^{7\times 7}$ are

$$\mathbf{A} = \begin{bmatrix} 1 & 0^{1\times 3} & 0^{1\times 3} \\ 0^{3\times 1} & \mathbf{I}^{3\times 3} & T_s\mathbf{I}^{3\times 3} \\ 0^{3\times 1} & \mathbf{0}^{3\times 3} & \mathbf{I}^{3\times 3} \end{bmatrix},$$
$$\Gamma = \begin{bmatrix} 1 & 0^{1\times 3} & 0^{1\times 3} \\ 0^{3\times 1} & T_s^2\mathbf{I}^{3\times 3} & \mathbf{0}^{3\times 3} \\ 0^{3\times 1} & \mathbf{0}^{3\times 3} & T_s\mathbf{I}^{3\times 3} \end{bmatrix}.$$

The estimator sample time is T_s, and $v_k \in \mathbb{R}^{7\times 1}$ is a discrete-time process noise.

The estimator is developed around the measurements emerging in the equation (8). In particular, it incorporates aircraft acceleration, orientation, and LARS orientation. While aircraft thrust is not directly measured, it can still be determined through system identification, a detailed explanation of which will be provided in Section 5. Rearranging the equation (8) for known values

$$\underbrace{-\mathbf{R}_i^c\left(m_a\ddot{\eta}_a^i + \mathbf{R}_a^i\begin{bmatrix}0\\0\\F_t\end{bmatrix} + \begin{bmatrix}0\\0\\m_a g\end{bmatrix}\right)}_{y_F} = F_l d^c, \qquad (15)$$

yields the measurement equation for the tension force and tether angles

$$y_F = F_l d^c.$$

The remaining states, namely tether length and corresponding rate of change, are estimated based on the winch actuator angular position and velocity measurements

$$y_{\theta_w} = (l - l_0)/r_w,$$
$$y_{\dot{\theta}_w} = \dot{l}/r_w,$$

where l_0 is the initial tether length. Finally, this leads to the estimator measurement equation

$$y_e = \begin{bmatrix} y_F \\ y_{\theta_w} \\ y_{\dot{\theta}_w} \end{bmatrix}.$$

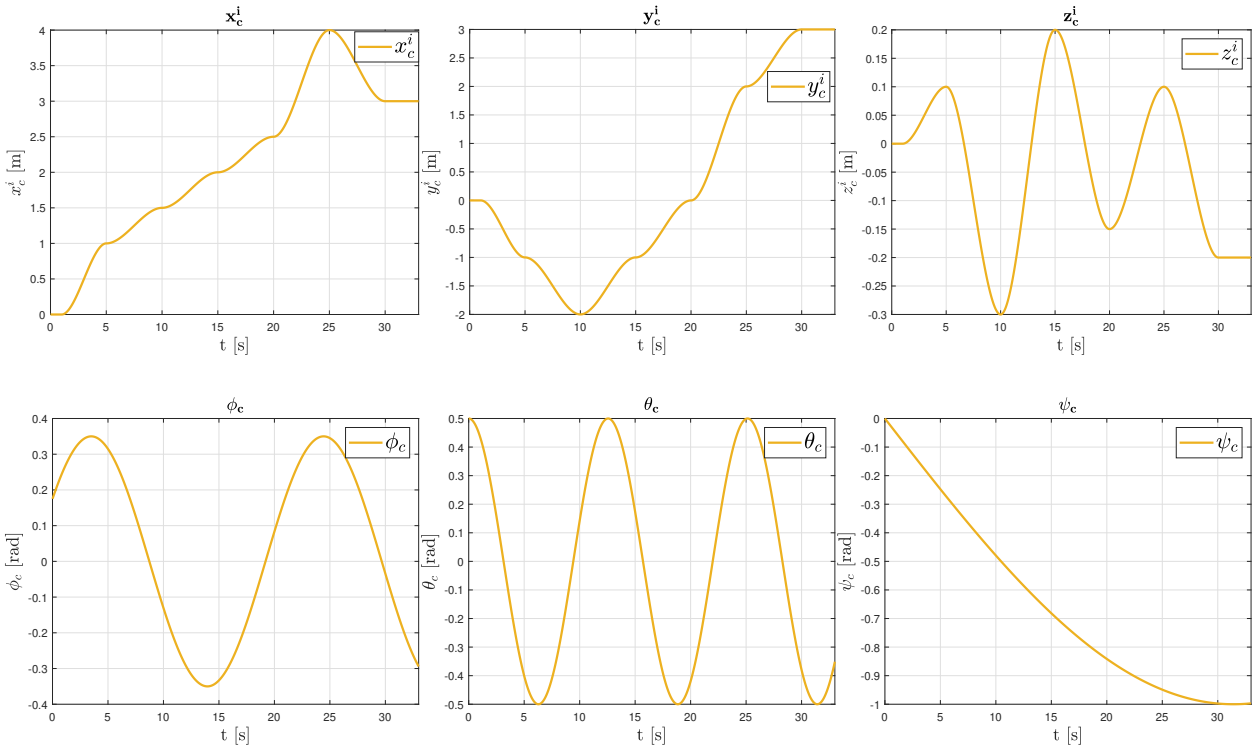


Figure 3: The position and orientation of the LARS mounted on a USV throughout the simulation. The oscillating roll, pitch and heave motion simulate the influence of waves.

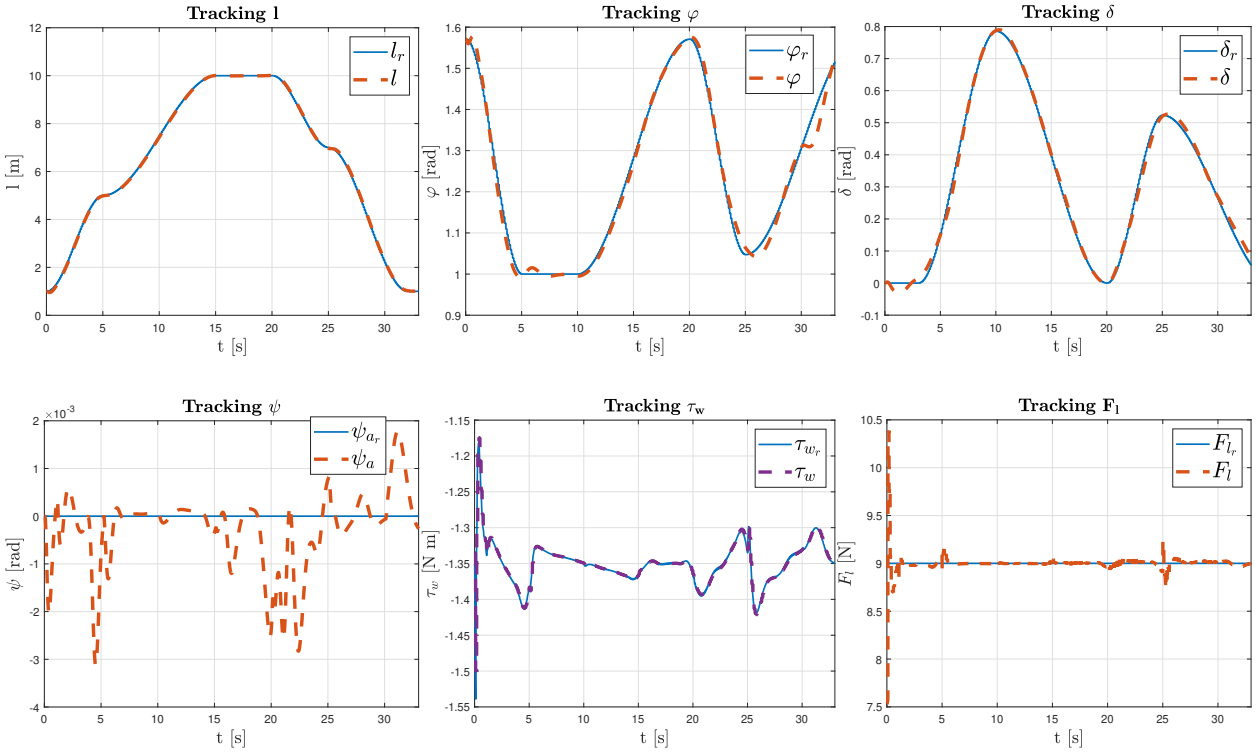


Figure 4: Tracking results for the simulated inputs (purple dashed) and outputs (red dashed), for the given reference trajectories (blue), in the simulation scenario where the simulated outputs are used for the control feedback.

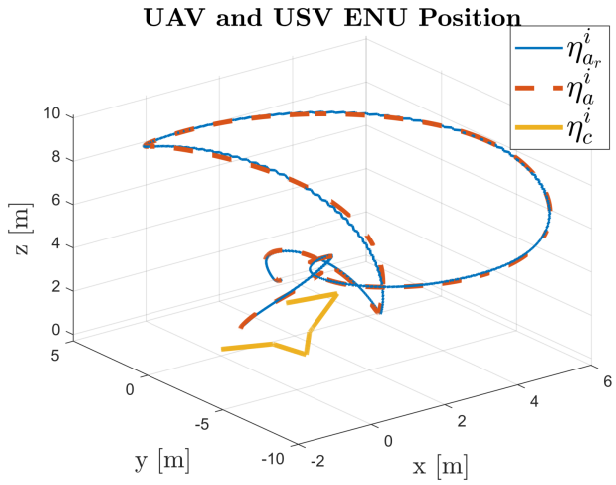


Figure 5: Simulated UAV (red dashed) and LARS (yellow) positions in ENU world frame. Depicted reference trajectory (blue) represents q references transformed to ENU world frame.

4.2. Numerical simulation

The estimator outlined in the previous sub-section controller is implemented in MATLAB®SIMULINK with the Control System Toolbox [31]. With the intention of creating a more faithful representation of real-world conditions, the measurements employed by the estimator were corrupted by the white noise. In the numerical simulation, the USV and UAV replicate the earlier trajectories. The Fig. 6 illustrates both the simulated states and their estimates, indicated by the hat symbol ($\hat{}$).

4.2.1. Tension force control for improved estimation

The measurements employed for the estimation can be considerably degraded by the noise, as showcased earlier. This has the potential to significantly influence the outcome of the estimation. The problem is accentuated when the signal-to-noise ratio further deteriorates due to the small tether force magnitude. To address this issue, tension force control can be utilized to increase the force magnitude. Several numerical simulations are performed for various reference tension forces F_{l_r} to demonstrate the effectiveness of this approach. The root-mean-squared error (RMSE) between the simulated and estimated states, along with the cumulative errors, are calculated and presented in Table 3. Reduction of error with increased tether tension force is observed, notably in φ and δ.

5. Experimental Setup and Implementation Details

For the experimental validation of the proposed algorithms, it is essential to consider several key factors. These include system parameter uncertainties, the need for real-time execution, and the constraints imposed by the existing low-level control structures on the experimental platform. The following subsections will introduce the experimental platform and provide implementation details of the control and estimation algorithms, ensuring that they align with these considerations.

Table 3: State estimation RMSE for different F_{l_r}

F_{l_r}	3 N	6 N	9 N	Unit
F_l	0.327	0.325	0.324	N
l	0.005	0.005	0.005	m
φ	0.033	0.019	0.014	rad
δ	0.061	0.036	0.026	rad
$\dot{l}$	0.019	0.019	0.019	$\mathrm{m\,s^{-1}}$
$\dot{\varphi}$	0.134	0.112	0.100	$\mathrm{rad\,s^{-1}}$
$\dot{\delta}$	0.191	0.158	0.141	$\mathrm{rad\,s^{-1}}$
$\sum$	0.769	0.672	0.629	

5.1. Experimental platform

The experimental platform consists of three primary components: the UAV, the LARS, and the Ground Control Station (GCS). An image of the experimental platform captured during the experimental verification is shown in Fig. 7.

5.1.1. UAV

The aerial platform used for experimental validation is the DJI Matrice 210v2 RTK. This UAV is equipped with a Manifold 2G onboard computer running Ubuntu 16.04 and ROS Kinetic. The DJI ONBOARD SDK[32] software package provides access to the aircraft's sensor data and integrated controllers, which include position, velocity, and attitude control. In addition to the onboard sensor suite, a load cell sensor is installed to provide cable tension measurements.

5.1.2. LARS

The main element of the LARS is the Brushless Direct Current (BLDC) actuator. This motor features an integrated controller with position, velocity, and torque operating modes. It utilizes a magnetic multi-turn absolute encoder for position and velocity feedback, offering a 17-bit single-turn and 16-bit multi-turn encoder resolution. The motor shaft is coupled to the cable reel, which houses the UAV tether. The motor is interfaced with the rest of the system via the LARS onboard computer. The LARS position and attitude measurements are provided by Pixhawk Autopilot which receives GPS-RTK input from the Emlid Reach M2 module.

5.1.3. GCS

The Ground Control Station is the primary platform for implementing control and estimation algorithms, operating on Ubuntu 20.04 with ROS Noetic. The algorithms are developed in MATLAB®SIMULINK. Data exchange between the GCS, LARS, and UAV is managed via the ROS network.

5.2. Controller formulation

To facilitate the implementation of the proposed NMPC on a real-world system, several modifications were necessary. A kinematic plant model was employed in place of the dynamic model, enabling real-time execution and removing the need for system parameters that are challenging to identify reliably, such as aircraft and winch actuator inertia. Additionally, this

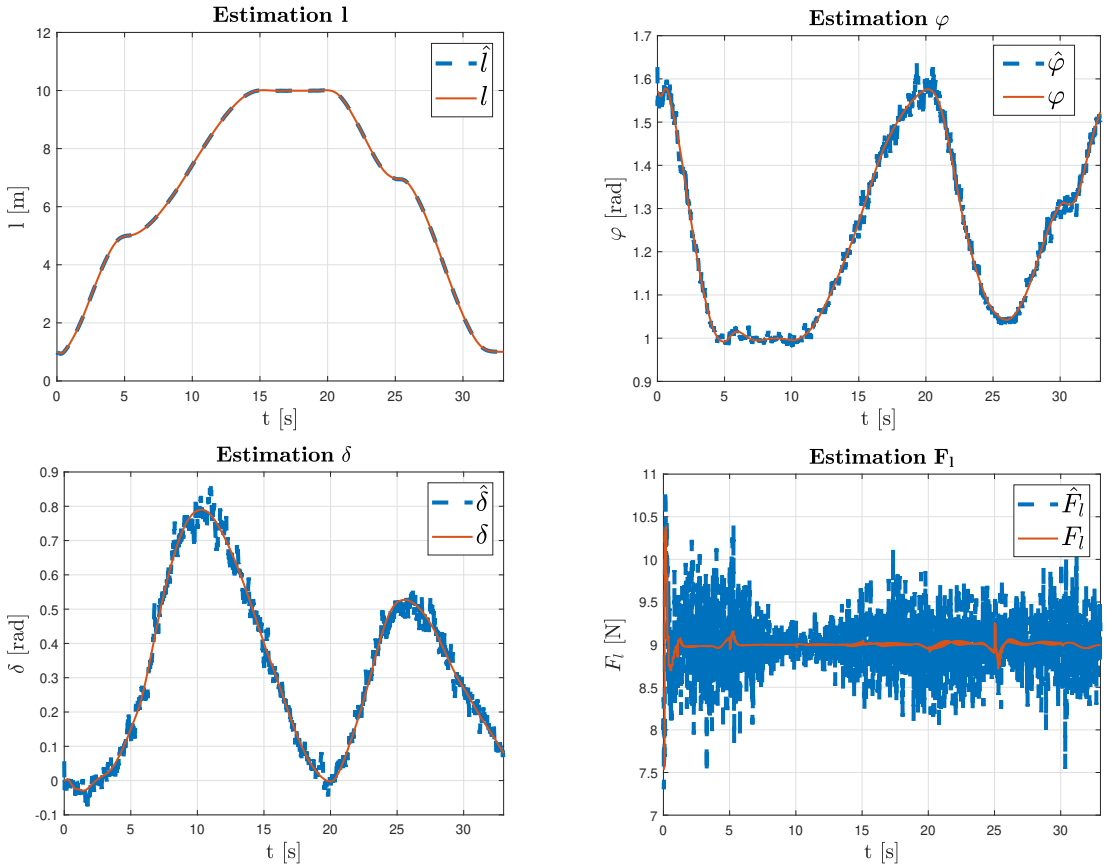


Figure 6: Actual states (red), and the estimated system states (blue dashed) in the numerical simulation.

approach allowed us to directly leverage the UAV's existing low-level control structure, whose model was experimentally determined through system identification. The controller performance was then evaluated, demonstrating accurate input reference tracking. Based on the performed analysis, the model of the onboard control structure was not included in the NMPC system model. This reduced overall model complexity and preserved the real-time execution capability of the NMPC algorithm. Subsequently, the new state vector $x \in \mathbb{R}^{3\times1}$, control input vector $u \in \mathbb{R}^{3\times1}$, vector of measured disturbances $d \in \mathbb{R}^{9\times1}$, and output vector $y \in \mathbb{R}^{3\times1}$ are defined as

$$x = q, \quad u = \dot{\eta}_a^i, \quad d = \begin{bmatrix} v_c^i & \xi_c & \omega_c^c \end{bmatrix}^T, \quad y = \mathbf{I}x \tag{16}$$

where $v_c^i = \mathbf{R}_c^i v_c^c$, and $\mathbf{I} \in \mathbb{R}^{3\times3}$ is the identity matrix. A new nonlinear plant model is derived from the kinematic relation (4) by solving the system of equations for q which yields

$$\dot{x} = f(x,u,d), \tag{17}$$

The set of new constraints and weights is specified in Table 4. The controller sample time was retained at 0.1 s, with prediction and control horizons set to 10 and 2 time steps, respectively.

While the NMPC handles trajectory tracking, cable tension control is delegated to a Proportional-Integral-Derivative (PID) controller running on the LARS onboard computer. This PID controller regulates tension by adjusting the torque of the LARS actuator based on load cell sensor measurements. Finally, the UAV yaw angle is controlled independently through the onboard SDK.

Table 4: NMPC Weights and Constraints for experimental validation

Output parameters				
x	w_y	x_{min}	x_{max}	Unit
l	5	0.1	50	m
φ	5	0	2π	rad
δ	5	$-\frac{\pi}{2}$	$\frac{\pi}{2}$	rad
Input parameters				
u	w_u	u_{min}	u_{max}	Unit
$\dot{\eta}_{a_x}$	0	-5	5	ms^{-1}
$\dot{\eta}_{a_y}$	0	-5	5	ms^{-1}
$\dot{\eta}_{a_z}$	0	-5	5	ms^{-1}

5.3. State estimation

State estimation relies heavily on accurate knowledge of the system parameters. While some parameters, such as aircraft mass, are readily available, others, like the aircraft thrust coefficient, must be determined experimentally. Additionally, assumptions made during modelling, such as a constant cable reel radius, may be valid in simulations but not in real systems.



Figure 7: Overview of the experimental platform. The LARS is located at the bottom centre of the image, while the tethered UAV is at the top left. The image was captured during the experimental verification at the Laboratory for Intelligent Autonomous Systems (LARIAT), University of Dubrovnik.

Therefore, system identification is necessary to correctly map encoder measurements for cable length estimation. The following subsections describe the identification and validation of these values as prerequisites for state estimation. Finally, the formulation of the Extended Kalman Filter used in the experimental verification is presented.

5.3.1. UAV thrust identification

The identification of UAV thrust is based on the velocity measurement of each quadrotor motor obtained through the onboard SDK. The interrelation of these quantities is described by the expression

$$\hat{F}_t = K_t \sum_{i=1}^{4} \omega_{m_i}^2, \tag{18}$$

where $K_t \in \mathbb{R}^+$ is the thrust coefficient to be evaluated by the identification, $\omega_{m_i} \in \mathbb{R}_0^+$ is the rotational velocity of each motor, and $\hat{F}_t$ is the estimated thrust force. Motor velocities are the

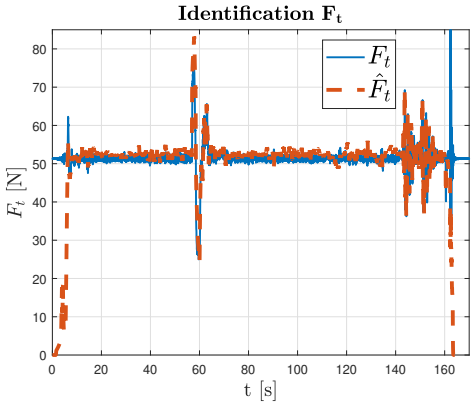


Figure 8: The UAV thrust calculated from the UAV measurements (blue) and estimated thrust based on the UAV quadrotor motor velocities and identified coefficient K_t (red dashed), in the 5.2 kg validation experiment.

input data for the identification. The output thrust data is calculated from the known aircraft mass and measured attitude and acceleration. To be specific, the aircraft transnational dynamics in the un-tethered free flight, given by the equation

$$m_a \ddot{\eta}_a^i = -\mathbf{R}_a^i \begin{bmatrix} 0 \\ 0 \\ F_t \end{bmatrix} - \begin{bmatrix} 0 \\ 0 \\ m_a g \end{bmatrix}.$$

The input and output data for the identification is collected in the series of un-tethered free flight experiments with the aircraft mass varied from 5.2 kg to 6.4 kg in the 0.4 kg increments. Through the identification process, the thrust coefficient is determined to be $K_t = 8.0889 \times 10^{-7}$. This value is verified on independent validation data for the above-mentioned aircraft masses. The measure of the goodness of fit between the modelled response and the output data is calculated using the normalized root mean square error (NRMSE) metric, defined by the expression

$$\text{FIT} = 100 \left(1 - \frac{\|y - \hat{y}\|}{\|y - \text{mean}\,(y)\|} \right),$$

where y represents the output data, and $\hat{y}$ denotes the modeled response. The fit values, expressed as a percentage for each validation experiment, are given in Table 5. The calculated and estimated thrust values for the 5.2 kg experiment are depicted in Fig. 8.

Table 5: K_t identification FIT values for varying m_a

m_a [kg]	FIT [%]
5.2	65.52
5.6	66.44
6.0	71.24
6.4	76.69

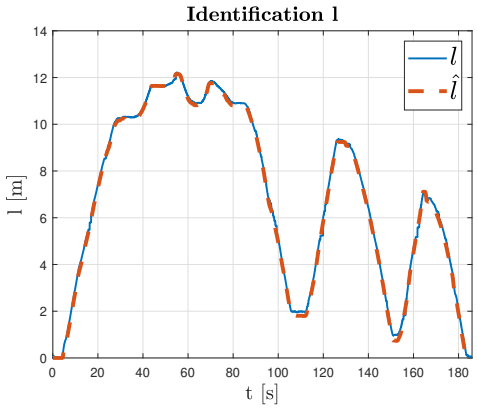


Figure 9: The cable length calculated from the GPS-RTK measurements (blue) and estimated cable length (red dashed), in the first validation experiment.

5.3.2. Cable length identification

Cable length identification is based on encoder measurements y_{θ_w}, and encoder resolution PPR. The number of motor revolutions is calculated from these values as

$$N_\theta = \frac{y_{\theta_w}}{PPR}.$$

The cable length is then determined by applying a least-squares optimization method to find the polynomial coefficients that minimize the error between the second-order polynomial and the motor revolutions measured at every 0.5 m increment along the tether length. The resulting polynomial is

$$\hat{l} = -0.00242\, N_\theta^2 + 0.71409\, N_\theta + 0.00383.$$

This model is verified in the three independent validation experiments, with the FIT values for each experiment given in Table 6. The ground truth cable length validation data is calculated using the ℓ_2 norm of the η_a^c position obtained from GPS-RTK measurements. The ground truth cable length and the estimated cable length for the first validation experiment are shown in Fig. 9.

Table 6: Cable length identification FIT values in three validation experiments

Experiment	FIT [%]
No. 1	96.55
No. 2	97.10
No. 3	96.27

5.3.3. Extended Kalman Filter

For the experimental validation, the estimator state $x_e \in \mathbb{R}^{8\times 1}$ is defined as

$$x_e = \begin{bmatrix} F_l & l & d^c & \dot{d}^c \end{bmatrix}^T.$$

A discrete white noise acceleration model represents the state transition of d^c, while the state transition of the tension force and cable length follows a random walk process. Consequently, the estimator process model is given as

$$x_{e_{k+1}} = \mathbf{A} x_{e_k} + \Gamma v_k, \tag{19}$$

where $\mathbf{A} \in \mathbb{R}^{8\times 8}$ and $\Gamma \in \mathbb{R}^{8\times 8}$ are

$$\mathbf{A} = \begin{bmatrix} 1 & 0 & 0^{1\times 3} & 0^{1\times 3} \\ 0 & 1 & 0^{1\times 3} & 0^{1\times 3} \\ 0^{3\times 1} & 0^{3\times 1} & \mathbf{I}^{3\times 3} & T_s\mathbf{I}^{3\times 3} \\ 0^{3\times 1} & 0^{3\times 1} & \mathbf{0}^{3\times 3} & \mathbf{I}^{3\times 3} \end{bmatrix},$$

$$\Gamma = \begin{bmatrix} 1 & 0 & 0^{1\times 3} & 0^{1\times 3} \\ 0 & 1 & 0^{1\times 3} & 0^{1\times 3} \\ 0^{3\times 1} & 0^{3\times 1} & T_s^2\mathbf{I}^{3\times 3} & \mathbf{0}^{3\times 3} \\ 0^{3\times 1} & 0^{3\times 1} & \mathbf{0}^{3\times 3} & T_s\mathbf{I}^{3\times 3} \end{bmatrix}.$$

The discrete-time process noise is denoted $v_k \in \mathbb{R}^{8\times 1}$, and T_s is the estimator sample time. The estimator is based on proprietary aircraft onboard sensor measurements and LARS encoder measurements. As in (15), acceleration and attitude measurements are utilized, along with the identified relation (18) for aircraft thrust. In contrast to the simulated model, the real-world implementation incorporates aircraft height measurement into the estimator. Using the kinematics equation (3), and assuming that the LARS height remains nearly constant $\left(\eta_{c_z}^i \approx 0\right)$, the height measurement equation is given by

$$y_z = \left(\mathbf{R}_c^i d^c l\right)_{(3)},$$

where y_z represents the third component of the resulting vector from the multiplication. Finally, by utilizing the identified relation for cable length, the set of estimator measurement equations is obtained as

$$y_e = \begin{bmatrix} y_{acc} & y_z & y_{\theta_w} \end{bmatrix}^T. \tag{20}$$

A comprehensive overview of the experimental setup and the implementation details of the proposed algorithms across the experimental platforms is depicted in Fig. 10.

6. Experimental validation

The experimental validation of the proposed control and estimation algorithms was conducted at the Laboratory for Intelligent Autonomous Systems (LARIAT), University of Dubrovnik. A series of experiments and subsequent analyses were performed to evaluate the effectiveness of these algorithms. The following section presents the results of one such experiment, with a video of the experiment available at [3].

During the experiment, the UAV was tasked with following a reference trajectory using a Nonlinear Model Predictive Control (NMPC). The control loop was closed using feedback from GPS-RTK measurements, which were transformed into controller states based on the kinematic transformations outlined in Section 2. These GPS-RTK measurements also served as ground truth information for tracking and estimation validation. The tension force control loop is closed utilizing the load cell measurements. The NMPC output tracking performance, as well as the PID tension force and the UAV yaw angle

[3] Experimental validation video - https://youtu.be/0qUJN51v54c

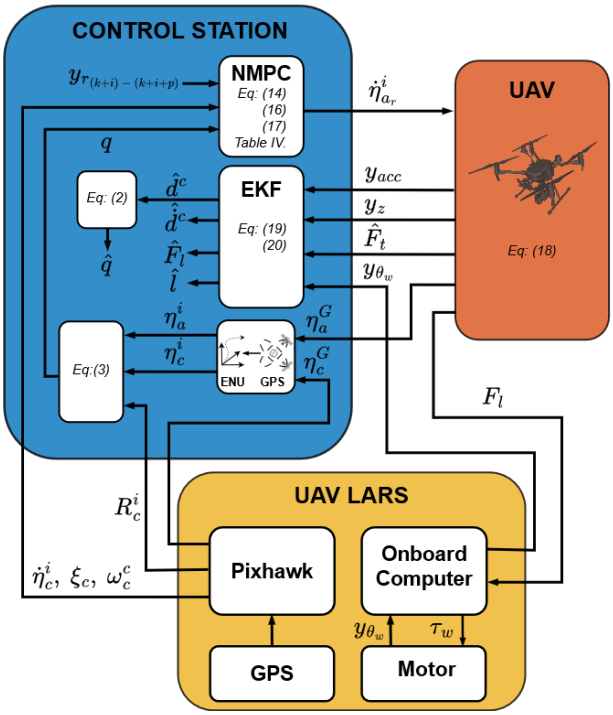


Figure 10: Overview of the experimental setup, highlighting the relevant signals and the distribution of the proposed control and estimation algorithms across the experimental platforms. The Control station processes measurements from both the UAV and the UAV LARS, executing the NMPC and EKF algorithms. The UAV receives trajectory tracking velocity references from the NMPC, while the UAV LARS regulates the tether tension.

tracking performance, are presented in Fig. 11. For a better visualization of the tracking performance, this figure also shows the tracking of the outputs presented in the ENU frame coordinates. The NMPC input tracking results, specifically UAV linear velocities $\dot{\eta}_a^i$ are depicted in Fig. 12. To demonstrate the controller's robustness against various measured disturbances, the LARS underwent a range of translational and attitude motions. The measured disturbances during the experiment, including the LARS linear velocity $\dot{\eta}_c^i$ and LARS Euler angles ξ_c are depicted in Fig. 15. The estimator performance with respect to the ground truth data is shown in Fig. 14, while proprietary onboard sensor measurements used as inputs for the EKF during the experiments are depicted in Fig. 13. The analysis of state estimation and tracking errors for the given experiment is summarized in Table 7. Additionally, the estimation errors for experiments with different reference tension values are analyzed and presented in Table 8.

The results demonstrate that the proposed NMPC can successfully track a given trajectory and effectively respond to measured disturbances. Except for a temporary loss of the GPS-RTK fix at the beginning of the experiment, tracking errors in azimuth and elevation angles did not exceed 0.0715 rad (4.1 degrees). The maximum length tracking error is 15 cm. The poorest tracking performance was observed in the tension force control, attributed to the narrow operating torque window of the actuator. This can be mitigated in the future by selecting a more suitable actuator and integrating the tension control into the NMPC structure.

The comparison between the estimates and ground truth data validates the proposed estimation workflow with minimal proprietary onboard sensing. As the data presented in Table 7 indicate, elevation and azimuth angle RMSE is 0.1 rad (5.7 degrees). This result is especially significant considering the level of noise present in the acceleration measurements as shown in Fig. 13. Furthermore, the estimation error is analyzed across three experiments, each with distinct reference tension forces of 8 N, 10 N, and 12 N, following the same reference trajectory. The observed reduction in estimation error with increasing reference tension force, detailed in Table 8, supports the utilization of tension force control in enhancing estimation accuracy.

Table 7: State estimation and tracking RMSE in the experimental validation

x	$(x-\hat{x})$	(x_r-x)	Unit
F_l	1.1283	2.4669	N
l	0.0335	0.0431	m
φ	0.0957	0.0204	rad
δ	0.1076	0.0208	rad
ψ_a	n/a	0.0085	rad

Table 8: State estimation RMSE for different F_{l_r} in the experimental validation

F_{l_r}	8 N	10 N	12 N	Unit
F_l	2.0880	1.2766	1.1283	N
l	0.0900	0.1073	0.0335	m
φ	0.1542	0.1008	0.0957	rad
δ	0.1239	0.1068	0.1076	rad
$\sum$	2.4561	1.5915	1.3651	

7. Conclusion

In this paper, a cooperative control framework for a tethered UAV system based on the Nonlinear Model Predictive Control (NMPC) method was presented. The effectiveness of the proposed control method was validated through a series of experiments, where the UAV demonstrated the accurate tracking of user-defined trajectories in the presence of external disturbances. The experimental results also highlighted how minimal proprietary sensing can be employed to estimate the UAV's relative position, even in scenarios involving translational and rotational LARS movements. It was further demonstrated that active interaction force control can enhance the estimation accuracy. Future work will focus on refining the control system, particularly by improving actuator selection for better interaction force control and integrating it into the model predictive control. In addition, efforts will be directed towards the modelling and prediction of the unmanned surface vehicle states to complement the existing estimation and control framework. Finally, the proposed framework will be assessed in the upcoming SeaClear2.0 project trials, where the UAV-LARS system will be deployed from an autonomous unmanned surface vehicle (USV) in a real-world operating environment.

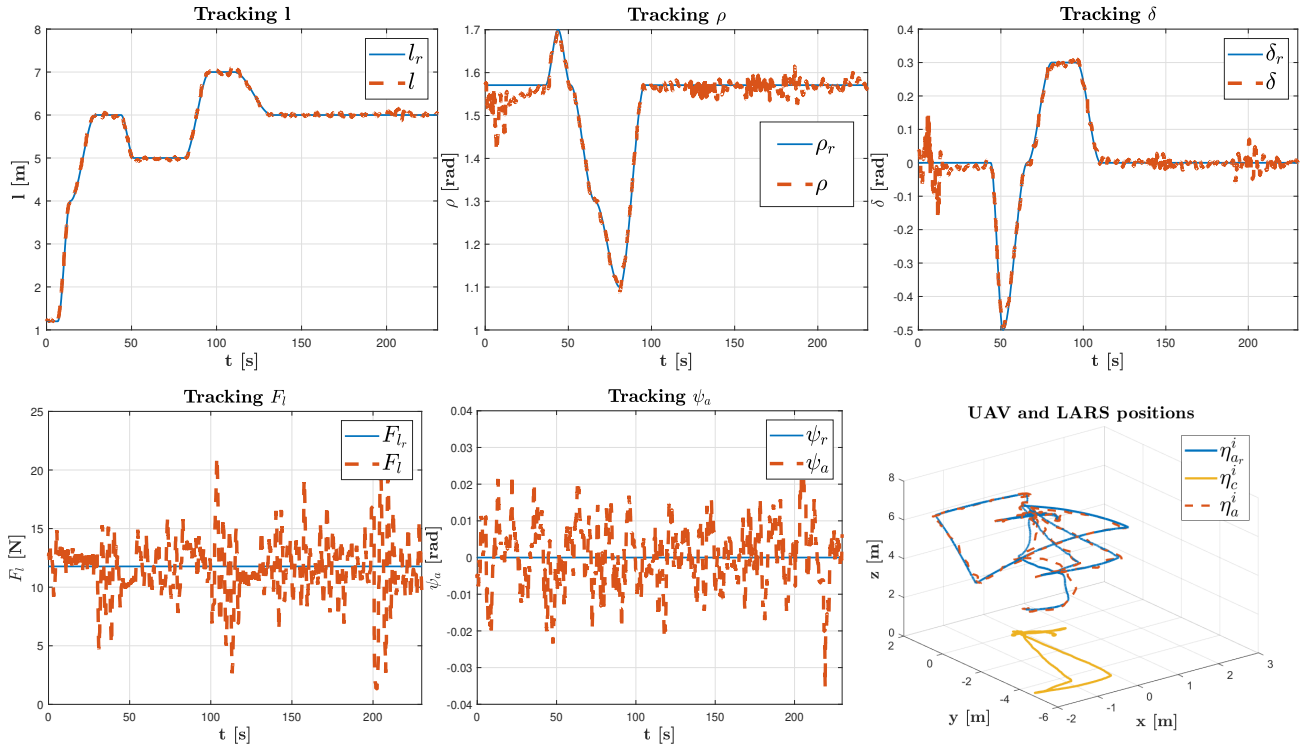


Figure 11: Output reference tracking results during experimental verification: output reference (blue) and ground truth outputs (red dashed). The final graph shows the LARS position (yellow), aircraft reference position (blue), and aircraft ground truth position (red dashed), given in the inertial reference frame during experimental verification.

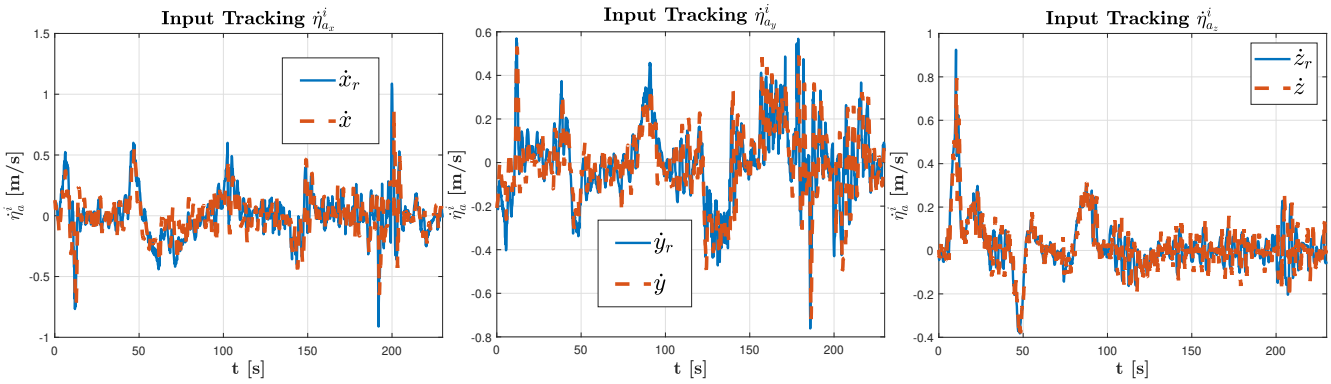


Figure 12: Input reference tracking results during experimental verification. Aircraft input velocity reference (blue) and ground truth aircraft velocity (red dashed).

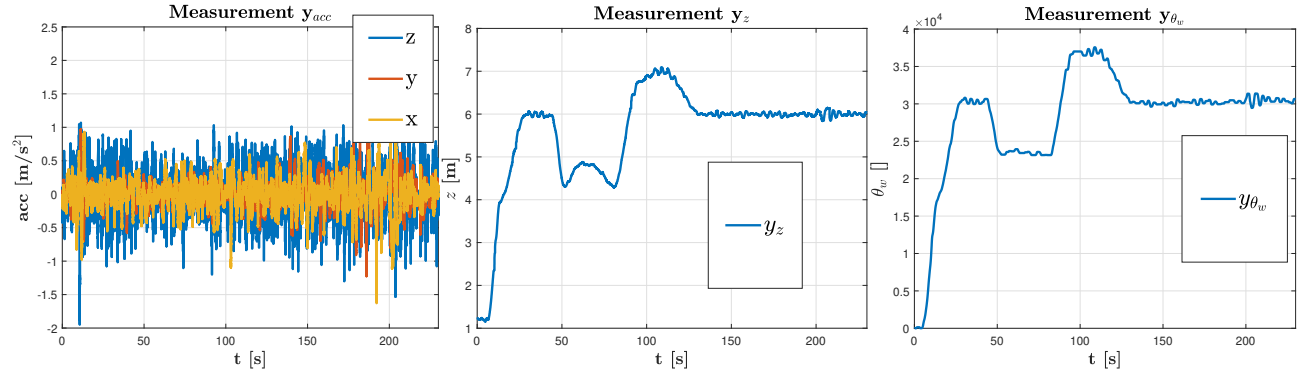


Figure 13: Measurement inputs for the Extended Kalman Filter during experimental verification: aircraft accelerations (left), aircraft altitude (middle), and LARS motor encoder readings (right).

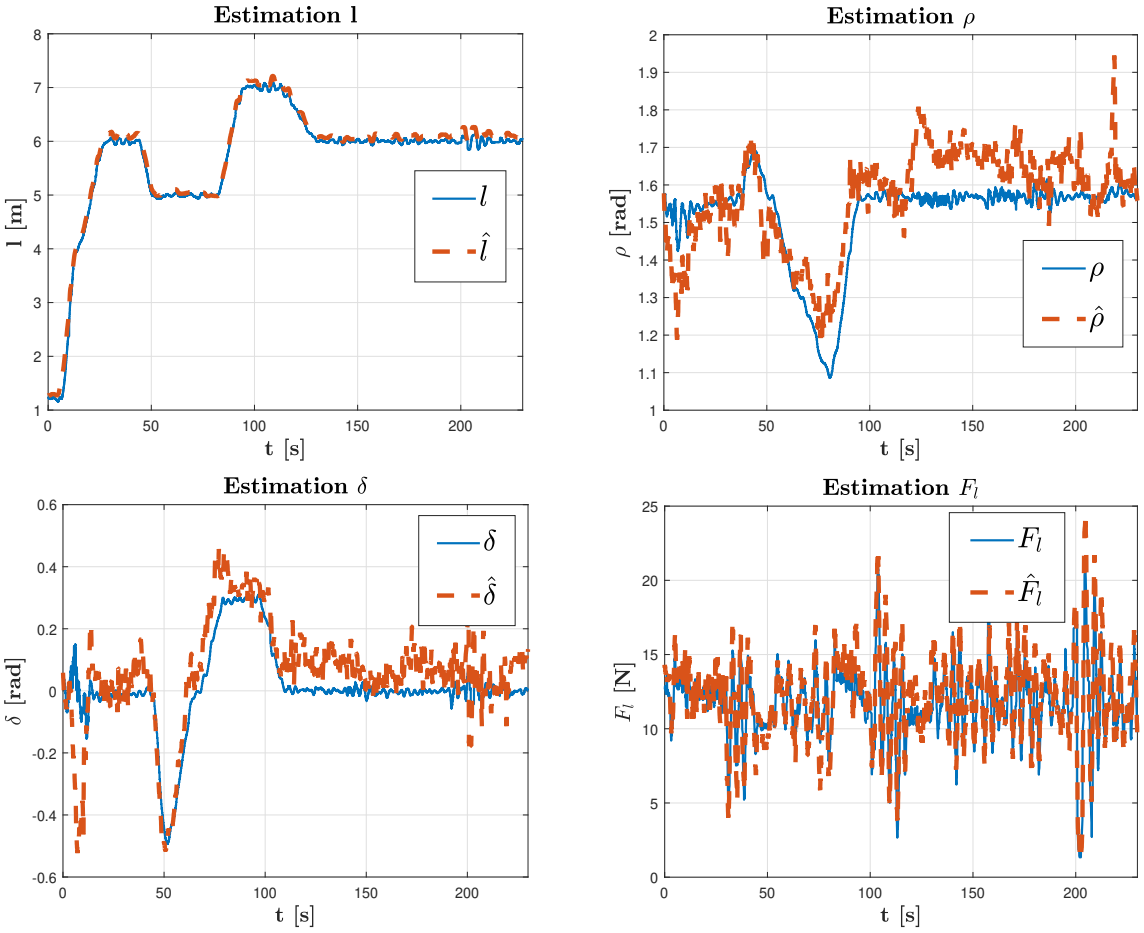


Figure 14: Ground truth system states (blue), and the estimated system states (red dashed) during experimental verification.

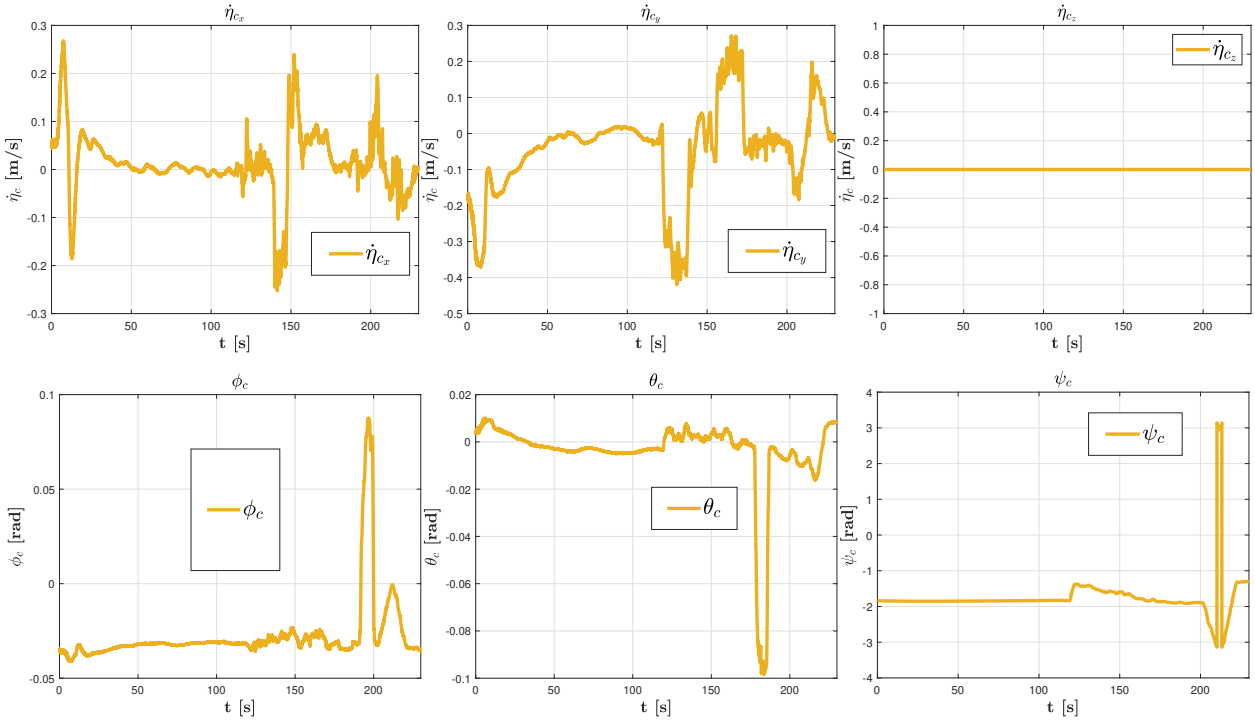


Figure 15: Measured disturbances during experimental verification: LARS velocity (top row), LARS Euler angles (bottom row).

CRediT authorship contribution statement

Vicko Prkačin: Conceptualization, Methodology, Software, Validation, Formal analysis, Investigation, Data Curation, Writing - Original Draft, Visualization. **Ivana Palunko:** Conceptualization, Methodology, Formal analysis, Resources, Writing - Review & Editing, Supervision, Project administration, Funding acquisition. **Ivan Petrović:** Writing - Review & Editing, Supervision.

Declaration of competing interest

The authors declare that they have no known competing financial interests or personal relationships that could have appeared to influence the work reported in this paper.

Acknowledgment

This work is supported by the European Union projects SeaClear (Horizon 2020, Grant No. 871295) and SeaClear2.0 (Horizon Europe, Grant No. 101093822).

The authors thank the reviewers for their insightful comments and suggestions, which contributed to the improvement of this paper.

References

[1] O. M. Bushnaq, M. A. Kishk, A. Celik, M.-S. Alouini, T. Y. Al-Naffouri, Optimal deployment of tethered drones for maximum cellular coverage in user clusters, IEEE Transactions on Wireless Communications 20 (3) (2021) 2092–2108. doi:10.1109/TWC.2020.3039013.

[2] B. W. Gu, S. Y. Choi, Y. S. Choi, G. Cai, L. Seneviratne, C. T. Rim, Novel roaming and stationary tethered aerial robots for continuous mobile missions in nuclear power plants, Nuclear Engineering and Technology 48 (4) (2016) 982–996. doi:https://doi.org/10.1016/j.net.2016.02.014.

[3] B. Galea, E. Kia, N. Aird, P. G. Kry, Stippling with aerial robots, in: Computational Aesthetics (Expressive 2016), 2016, p. 10 pages.

[4] K. S. Pratt, R. R. Murphy, J. L. Burke, J. Craighead, C. Griffin, S. Stover, Use of tethered small unmanned aerial system at berkman plaza ii collapse, in: 2008 IEEE International Workshop on Safety, Security and Rescue Robotics, 2008, pp. 134–139. doi:10.1109/SSRR.2008.4745890.

[5] L. A. Sandino, M. Béjar, K. Kondak, A. Ollero, Advances in modeling and control of tethered unmanned helicopters to enhance hovering performance, Journal of Intelligent & Robotic Systems 73 (2014) 3–18.

[6] T. Lee, Geometric controls for a tethered quadrotor uav, in: 2015 54th IEEE Conference on Decision and Control (CDC), 2015, pp. 2749–2754. doi:10.1109/CDC.2015.7402632.

[7] M. Tognon, S. S. Dash, A. Franchi, Observer-based control of position and tension for an aerial robot tethered to a moving platform, IEEE Robotics and Automation Letters 1 (2) (2016) 732–737. doi:10.1109/LRA.2016.2523599.

[8] M. Tognon, A. Franchi, Theory and Applications for Control of Aerial Robots in Physical Interaction Through Tethers, Tracts in Advanced Robotics, Springer, 2020. doi:10.1007/978-3-030-48659-4.

[9] K. Talke, M. De Oliveira, T. Bewley, Catenary tether shape analysis for a uav - usv team, in: 2018 IEEE/RSJ International Conference on Intelligent Robots and Systems (IROS), 2018, pp. 7803–7809. doi:10.1109/IROS.2018.8594280.

[10] K. Talke, F. Birchmore, T. Bewley, Autonomous hanging tether management and experimentation for an unmanned air-surface vehicle team, Journal of Field Robotics 39 (6) (2022) 869–887. doi:https://doi.org/10.1002/rob.22083.

[11] R. R. Lima, B. Martinez Rocamora, G. A. S. Pereira, Continuous vector fields for precise cable-guided landing of tethered uavs, IEEE Robotics and Automation Letters 8 (7) (2023) 4370–4377. doi:10.1109/LRA.2023.3281940.

[12] D. Falanga, A. Zanchettin, A. Simovic, J. Delmerico, D. Scaramuzza, Vision-based autonomous quadrotor landing on a moving platform, in: 2017 IEEE International Symposium on Safety, Security and Rescue Robotics (SSRR), 2017, pp. 200–207. doi:10.1109/SSRR.2017.8088164.

[13] T. K. Venugopalan, T. Taher, G. Barbastathis, Autonomous landing of an unmanned aerial vehicle on an autonomous marine vehicle, in: 2012 Oceans, 2012, pp. 1–9. doi:10.1109/OCEANS.2012.6404893.

[14] S. Kiribayashi, K. Yakushigawa, K. Nagatani, Position estimation of tethered micro unmanned aerial vehicle by observing the slack tether, in: 2017 IEEE International Symposium on Safety, Security and Rescue Robotics (SSRR), 2017, pp. 159–165. doi:10.1109/SSRR.2017.8088157.

[15] X. Xiao, Y. Fan, J. Dufek, R. Murphy, Indoor uav localization using a tether, in: 2018 IEEE International Symposium on Safety, Security, and Rescue Robotics (SSRR), 2018, pp. 1–6. doi:10.1109/SSRR.2018.8468627.

[16] A. Borgese, D. C. Guastella, G. Sutera, G. Muscato, Tether-based localization for cooperative ground and aerial vehicles, IEEE Robotics and Automation Letters 7 (3) (2022) 8162–8169. doi:10.1109/LRA.2022.3187504.

[17] F. Alarcón, M. García, I. Maza, A. Viguria, A. Ollero, A precise and gnss-free landing system on moving platforms for rotary-wing uavs, Sensors 19 (4) (2019). doi:10.3390/s19040886.

[18] B. Martinez Rocamora, R. R. Lima, K. Samarakoon, J. Rathjen, J. N. Gross, G. A. S. Pereira, Oxpecker: A tethered uav for inspection of stonemine pillars, Drones 7 (2) (2023). doi:10.3390/drones7020073.

[19] S. Lupashin, R. D'Andrea, Stabilization of a flying vehicle on a taut tether using inertial sensing, in: 2013 IEEE/RSJ International Conference on Intelligent Robots and Systems, 2013, pp. 2432–2438. doi:10.1109/IROS.2013.6696698.

[20] A. Al-Radaideh, L. Sun, Self-localization of a tethered quadcopter using inertial sensors in a gps-denied environment, in: 2017 International Conference on Unmanned Aircraft Systems (ICUAS), 2017, pp. 271–277. doi:10.1109/ICUAS.2017.7991436.

[21] V.-M. Maer, Z. Lendek, S. Přrje, D. Tolić, A. Đuraš, V. Prkačin, I. Palunko, L. Busoniu, Two-channel extended kalman filtering with intermittent measurements, in: 2024 American Control Conference (ACC), 2024, pp. 1204–1211. doi:10.23919/ACC60939.2024.10644674.

[22] A. Đuraš, M. Sukno, I. Palunko, Recovering the 3d uuv position using uav imagery in shallow-water environments, in: 2022 International Conference on Unmanned Aircraft Systems (ICUAS), 2022, pp. 948–954. doi:10.1109/ICUAS54217.2022.9836195.

[23] T. Baca, P. Stepan, V. Spurny, D. Hert, R. Penicka, M. Saska, J. Thomas, G. Loianno, V. Kumar, Autonomous landing on a moving vehicle with an unmanned aerial vehicle, Journal of Field Robotics 36 (5) (2019) 874–891. doi:https://doi.org/10.1002/rob.21858.

[24] P. M. Gupta, E. Pairet, T. Nascimento, M. Saska, Landing a uav in harsh winds and turbulent open waters, IEEE Robotics and Automation Letters 8 (2) (2023) 744–751. doi:10.1109/LRA.2022.3231831.

[25] L. Fagiano, Systems of tethered multicopters: Modeling and control design, IFAC-PapersOnLine 50 (1) (2017) 4610–4615, 20th IFAC World Congress. doi:https://doi.org/10.1016/j.ifacol.2017.08.653.

[26] F. Novák, T. Báča, M. Saska, Collaborative object manipulation on the water surface by a uav-usv team using tethers, in: 2024 IEEE/RSJ International Conference on Intelligent Robots and Systems (IROS), 2024, pp. 3425–3432. doi:10.1109/IROS58592.2024.10802469.

[27] V. Prkačin, I. Palunko, I. Petrović, State and parameter estimation of suspended load using quadrotor onboard sensors, in: 2020 International Conference on Unmanned Aircraft Systems (ICUAS), 2020, pp. 958–967. doi:10.1109/ICUAS48674.2020.9213840.

[28] V. Prkačin, I. Palunko, I. Petrović, Extended kalman filter for payload state estimation utilizing aircraft inertial sensing, in: 2021 Aerial Robotic Systems Physically Interacting with the Environment (AIRPHARO), 2021, pp. 1–6. doi:10.1109/AIRPHARO52252.2021.9571038.

[29] The Mathworks, Inc., Model Predictive Control Toolbox R2022a (2022). URL https://www.mathworks.com/help/mpc/

[30] DJI, DJI M210 RTK V2 Manual (2019). URL https://www.dji.com/hr/matrice-200-series-v2/info

[31] The Mathworks, Inc., Control System Toolbox R2022a (2022). URL https://www.mathworks.com/help/control/

[32] DJI, DJI Onboard SDK (OSDK) 4.1.0 (2021). URL https://github.com/dji-sdk/Onboard-SDK